Multi-Disciplinary Design Optimization of an Electric Motor Considering Thermal Constraints

Tucker Babcock [*], Bryan McKeever [†], and Jason E. Hicken [‡]
Rensselaer Polytechnic Institute, Troy, NY, 12180

Numerical optimization can help inform the design of aircraft propulsive electric motors, but only if the motor's performance is predicted with sufficient accuracy. To address prediction accuracy, this paper presents a multi-disciplinary analysis model that accounts for losses in the machine as a function of frequency, flux density, and temperature. Additionally, we model demagnetization in the permanent magnets to further capture the effect of temperature on motor performance. We analytically compute derivatives through our multi-disciplinary analysis using coupled adjoints to ensure that we can use efficient gradient-based optimization methods. We then demonstrate the developed optimization framework on a realistic aerospace-grade electric motor optimization, demonstrating an increase in efficiency over the baseline design, while satisfying the motor's thermal and output power constraints.

I. Introduction

The aviation industry must reduce its environmental impact. Direct CO_2 emissions from the aircraft sector account for approximately 2.0-2.5 % of yearly global CO_2 emissions [1, 2], representing around 7 % of the world's oil-product consumption [3]. In addition, it is estimated that non-CO_2 aircraft emissions such as NO_x and H_2O, which can induce the formation of contrails and contrail-cirrus clouds, may account for just as much of a warming effect on the planet as aircraft CO_2 emissions [4, 5]. Further, NO_x and other aerosol emissions are known to cause local air-quality hazards that may contribute to premature deaths in communities near airports [6].

As battery technology has and continues to develop, electric and hybrid-electric propulsion systems are considered compelling options among the possible paths to reduced emissions, particularly for commuter and short-haul routes [3, 7, 8]. For example, Brelje and Martins [9] suggest that electric propulsion can help civil aircraft meet the aggressive N+3 performance goals put forth by NASA, which are characterized by stringent emissions, noise, and fuel burn requirements [10].

While there are many challenges associated with the electrification of aircraft, we focus on the analysis and optimization of their electric motors. The analysis of electric motors suitable for aircraft applications demands a multi-disciplinary analysis (MDA) that considers the electromagnetic and thermal coupling in the motor. This coupled analysis is essential, as the motor's performance depends heavily on its temperature. This coupling is particularly important during takeoff, where high power requirements produce significant heating in the motor's windings and core. For example, a trajectory optimization study by Falck *et al.* [11] predicted that thermal constraints on the electric motors in NASA's X-57 aircraft would limit its rate of climb. If these thermal constraints are violated, the motor will experience adverse performance as the permanent magnets suffer demagnetization, and may even fail catastrophically if the winding insulation breaks down and causes short circuits. Further, the authors of [11] noted that if the motors were optimized alongside the trajectory, they could use lower-power motors than originally specified, resulting in lighter motors that did not hit their thermal constraints, and thus would not limit the overall trajectory.

The field of multi-disciplinary electric motor analysis is quite mature; there are numerous commercial software tools available to engineers, such as Ansys's MotorCAD [12] and Maxwell [13] and Altair's Flux [14] and FluxMotor [15], that offer multi-disciplinary analysis capabilities at mid- and high-fidelity. In addition to the commercial tools available, there are ongoing research efforts to better model the multi-disciplinary coupling between the electromagnetic and thermal behavior of a motor. Several methods have been developed to model the effects of permanent magnet demagnetization so that the behavior may be accurately computed during analysis and optimization, including piecewise linear [16–18] and transcendental [18–22] fits of experimental data. The modeling of the temperature dependence of electromagnetic losses has received similar attention. It is well understood that the electrical conductivity of commonly used conductors

---

[*]Ph.D. Candidate, Department of Mechanical, Aerospace, and Nuclear Engineering; Student Member AIAA.
[†]Graduate Student, Department of Mechanical, Aerospace, and Nuclear Engineering; Student Member AIAA.
[‡]Associate Professor, Department of Mechanical, Aerospace, and Nuclear Engineering; Associate Fellow AIAA.

is adversely affected by increasing temperature, which in turn affects both the direct-current (DC) and alternating-current (AC) losses [23]. On the other hand, the influence of temperature on core losses in the motor's steel due to eddy-current and hysteresis effects are frequently not considered [24–30]. Xue *et al.* [31] recently introduced a temperature-dependent core loss model that separates the eddy-current and hysteresis terms and uses nonlinear coefficient functions on each to accurately capture core losses over a spectrum of temperatures, frequencies, and magnetic flux densities [32].

Several studies have built on the methods developed to consider the temperature dependence of electromagnetic analysis, and have considered fully-coupled electro-thermal motor analysis, using a combination of commercial and research codes [27, 33–36]. Further, there have been various optimization studies conducted using gradient-free algorithms to optimize motors subject to thermal constraints [37–44]. Unfortunately, the poor algorithmic scaling of gradient-free optimization algorithms limits the number of design variables that may be considered in the optimization [45], limiting the potential improvement that can be realized from the optimization. In addition, closed-source motor analyses that do not provide derivative information may preclude the inclusion of the motor model in a larger system-level optimization study. For problems with many (> 10) design variables, gradient-based optimization algorithms supplied with analytically computed gradients are required for the optimization to remain efficient [46, 47].

This paper details the development of a fully-coupled electro-thermal motor analysis and gradient-based optimization framework. This framework builds upon our previous work [48] and considers temperature-dependent magnetization and loss models, and analytically computes derivatives through the coupled nonlinear model using coupled adjoints. While there has been considerable work using coupled adjoints for aero-structural optimization [49–52], aero-propulsive optimization [53–55], and conjugate heat transfer optimization [56, 57], to the best of our knowledge there has not been any work that has used coupled adjoints for electro-thermal optimization. Thus, the main contribution of this work is the application of coupled adjoints to compute derivatives through the coupled electro-thermal motor analysis. By computing derivatives through our coupled multi-disciplinary motor analysis, we enable the use of efficient gradient-based optimization algorithms for coupled electro-thermal motor problems.

The remainder of this paper is organized as follows. Section II describes the parameterization of the motor, along with the electromagnetic and thermal analyses. In particular, we describe the models for temperature-dependent losses and permanent magnet demagnetization. Section III describes our fully-coupled electro-thermal multi-disciplinary analysis, and covers how we efficiently compute derivatives through it. Section IV presents optimization results, considering both feedforward and feedback electro-thermal coupling. Finally, Section V concludes the paper with a summary and discussion.

II. Methods

This section describes the physical models used in the motor modeling framework and the assumptions that motivate the models. We first discuss the parameterization of the motor geometry, then the electromagnetic analysis, and finally the thermal analysis.

A. Motor Parameterization

Among the several electric motor architectures suitable for aerospace applications, we consider the three-phase radial-flux inrunner permanent magnet synchronous motor (PMSM) in this work. We characterize the continuous geometry of the PMSM with the parameters listed in Table 1 and illustrated in Fig. 1. Note that the stack length is an "out-of-the-page" parameter measuring the axial depth of the motor and is thus not shown in Fig. 1.

In addition to the geometric parameters listed in Table 1, we characterize the PMSM by an additional set of continuous parameters listed in Table 2, which we briefly describe here. In a PMSM, each phase of the motor has a round wire with radius r_s. The wire is wrapped around a stator tooth n_t times, and has an alternating-current (AC) with root-mean-squared (RMS) value i flowing through it. Finally, the rotor's rotations per minute (RPM) are directly related to the frequency of the motor's AC current f_e as $S = \frac{60}{n_p} f_e$, where n_p is the number of magnetic poles on the rotor.

On top of the continuous parameters already discussed, the design of a PMSM requires the selection of several discrete parameters, which are also listed in Table 2. The number of magnetic poles on the rotor and the number of winding slots in the stator are two discrete design choices that significantly impact the motor's behavior. Additionally, the material choices for each component can dramatically influence the optimal PMSM design. As we are using gradient-based optimization for our motor optimization framework, we cannot directly optimize over these discrete parameters. This is not a tremendous issue, however, since electric-motor design theory provides guidance for such discrete parameter selection [58].
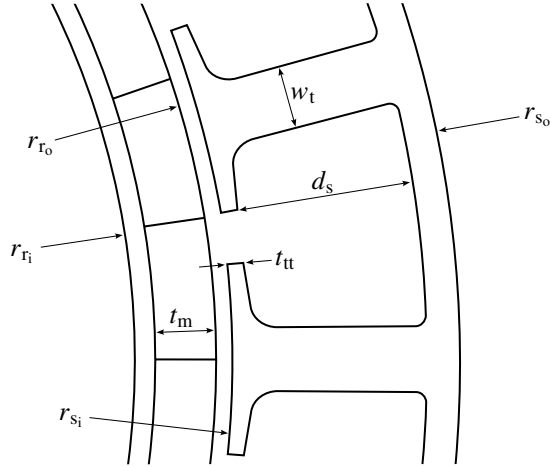
Fig. 1 **Diagram showing how geometric design parameters define the geometry for the PMSM of interest.**

Table 1 **Continuous motor geometric design parameters and their physical descriptions.**

Parameter	Description
l_s	Stack length
d_s	Slot depth
t_m	Magnet thickness
r_{r_i}	Rotor inner radius
r_{r_o}	Rotor outer radius
r_{s_i}	Stator inner radius
r_{s_o}	Stator outer radius
w_t	Tooth width
t_{tt}	Tooth tip thickness

Table 2 **Remaining motor design parameters and their physical descriptions.**

Parameter	Description	Classification
r_s	Strand radius	Continuous
i	RMS current	Continuous
S	Rotor RPM	Continuous
n_t	Number of winding turns	Discrete
n_p	Number of magnetic poles	Discrete
n_s	Number of stator slots	Discrete

3

B. Computational Geometry Model

We use the Engineering Sketch Pad (ESP) [59] parametric CAD system to represent the PMSM geometry in the model, with the design parameters listed in Table 1. We use the EGADS Tessellator [60] through the CAPS [61] interface to generate the finite-element meshes needed by the electromagnetic and thermal analyses. Finally, we use EGADS' tesselation APIs [60] to explicitly map changes in the geometric design parameters identified in Table 1 to changes in mesh node coordinates of the a priori generated finite-element meshes as the design parameters are updated throughout the optimization process. We use x^h to denote the mesh node coordinates.

C. Electromagnetic Analysis

This section describes the electromagnetic field model used for the analysis, and it details the electromagnetic outputs we compute. We further highlight the effect of temperature dependence on both the electromagnetic field solution and the outputs we compute.

1. Electromagnetic Field Model

We model the electromagnetic field in the motor with the magnetostatic simplification of Maxwell's equations, given in differential form as

$$\nabla \times \boldsymbol{H} = \boldsymbol{J}_{\text{src}}, \qquad \forall \, \boldsymbol{x} \in \Omega_{\text{E}}, \tag{1}$$

$$\nabla \cdot \boldsymbol{B} = 0, \qquad \forall \, \boldsymbol{x} \in \Omega_{\text{E}}, \tag{2}$$

where $\boldsymbol{H} \in \mathbb{R}^{\text{d}}$ is the magnetic field intensity, $\boldsymbol{J}_{\text{src}} \in \mathbb{R}^{\text{d}}$ is the current density from applied sources, $\boldsymbol{B} \in \mathbb{R}^{\text{d}}$ is the magnetic flux density, and d is the spatial dimension. The set Ω_{E} denotes the computational domain of the electromagnetic analysis, taken here to be a two-dimensional cross-section of the motor. Equations (1) and (2) are known as Ampère's circuital law and Gauss's law for magnetism, respectively. Equations (1) and (2) need boundary conditions to define a well-posed boundary value problem; these will be discussed shortly.

The magnetic field intensity, $\boldsymbol{H}$, and the magnetic flux density, $\boldsymbol{B}$, are related through the following constitutive equation:

$$\boldsymbol{H} = \nu \left(\boldsymbol{B} \right) \left(\boldsymbol{B} - \boldsymbol{M}(T) \right), \tag{3}$$

where $\nu \left(\boldsymbol{B} \right)$ is the reluctivity, and $\boldsymbol{M}(T)$ is the temperature-dependent magnetic source created by permanent magnets. In general, the reluctivity is a material-dependant nonlinear function of the magnetic flux density. We discuss the details of the reluctivity model we use in Appendix A. We follow the approach described by Chen *et al.* [62] and model the magnetic source as the linear function of temperature

$$\boldsymbol{M}(T) = \boldsymbol{M}_0 \left(1 - \alpha_{\boldsymbol{M}} \left(T - T_{\boldsymbol{M},0} \right) \right), \tag{4}$$

where $\boldsymbol{M}_0$, $\alpha_{\boldsymbol{M}}$ and $T_{\boldsymbol{M},0}$ are material-specific parameters provided in manufacturer datasheets. We take $\boldsymbol{M}_0 = 1.39$ T, $\alpha_{\boldsymbol{M}} = -1.2 \times 10^{-3} \, \frac{1}{\text{K}}$ and $T_{\boldsymbol{M},0} = 293.15$ K for the $\text{Nd}_2\text{Fe}_{14}\text{B}$ magnets considered in this work [63].

We use the magnetic vector potential, $\boldsymbol{A} \in \mathbb{R}^{\text{d}}$, defined to satisfy

$$\boldsymbol{B} = \nabla \times \boldsymbol{A}, \tag{5}$$

such that Eq. (2) is satisfied by construction. Equation (5) does not uniquely define $\boldsymbol{A}$, as the gradient of any scalar function may be added to $\boldsymbol{A}$ without changing $\boldsymbol{B}$. We remedy this by imposing the Coulomb gauge $\nabla \cdot \boldsymbol{A} = 0$ on $\boldsymbol{A}$.

Using this gauge condition, the magnetic vector potential from Eq. (5), the constitutive relation defined in Eq. (3), and by restricting the $\boldsymbol{B}$ field to be two-dimensional, Eq. (1) can be re-written as the following nonlinear scalar diffusion equation for the z-component of $\boldsymbol{A}$:

$$-\nabla \cdot \left(\nu \left(\boldsymbol{B} \right) \nabla A_{\text{z}} \right) - \left[\nabla \times \left(\nu \boldsymbol{M} \left(T \right) \right) \right]_{\text{z}} - J_{\text{src}_{\text{z}}} = 0, \qquad \forall \, \boldsymbol{x} \in \Omega_{\text{E}}. \tag{6}$$

Here, $J_{\text{src}_{\text{z}}}$ is a piecewise-continuous source, which is non-zero only in the part of the domain containing the motor's windings and represents the applied current density. To ensure a well-posed boundary value problem, we implement Dirichlet boundary conditions on Eq. (6), imposing that $A_{\text{z}} = 0$ along the entire boundary of Ω_{E}. This is equivalent to enforcing that $\boldsymbol{B} \cdot \hat{\boldsymbol{n}} = 0$ along the boundary, i.e. that there is no flux fringing.

We use the Modular Finite Element Methods (MFEM) [64, 65] library to discretize Eq. (6) with the finite-element method. This results in the following algebraic form:

$$\boldsymbol{R}_A = \boldsymbol{R}_A(A^h, x^h, T^h, \boldsymbol{J}) = \boldsymbol{0}, \tag{7}$$

where A^h is the vector of finite-element degrees of freedom, x^h is the vector of mesh node coordinates, and T^h is the vector of temperature values at each finite-element degree of freedom. $J \in \mathbb{R}^p$ holds the z-axis-aligned current density J_{src_z} for each of the p phases in the motor. We solve Eq. (7) multiple times at different rotor positions to capture the behavior of the motor at different points in time. This will be discussed in more detail shortly.

We solve Eq. (7) for A^h using Newton's method with a backtracking line search that ensures that $\|R_A\|$ decreases at each iteration (see, for example, [47, Chapter 4.3.3]). Each Newton update is computed using the preconditioned conjugate gradient (PCG) method, preconditioned with the "BoomerAMG" algebraic multigrid (AMG) preconditioner from the *hypre* library [66, 67]. We use relative and absolute tolerances of 10^{-6} as the convergence criteria for the Newton iterations, and we use a relative and absolute linear solver tolerance of 10^{-12} when solving the Newton updates. We use default settings for the BoomerAMG preconditioner in *hypre* version 2.25.0.

2. Electromagnetic Outputs Including Losses

Once the solution to Eq. (7) has been computed we can calculate the motor's performance outputs, as well as the loss terms that account for reductions in efficiency and increases in temperature. We consider losses caused by direct current (DC) and alternating current (AC) known as copper losses. We also model losses caused by hysteresis and eddy currents in the motor's magnetic steel (in the stator and the rotor) known as core losses. We consider the effects of temperature on each loss term we model.

To calculate the DC losses, we first compute the length of a conductor winding l_{w} in one of the motor's p phases as

$$l_{\text{w}} = 2n_{\text{t}} \frac{n_{\text{s}}}{p} \left(l_{\text{s}} + \pi \left(\frac{w_{\text{t}}}{2} + \frac{\pi \left(2r_{\text{s}_i} + d_{\text{s}} + t_{\text{tt}} \right)}{4n_{\text{s}}} \right) \right) + \frac{\pi \left(2r_{\text{s}_i} + d_{\text{s}} + t_{\text{tt}} \right)}{2}, \tag{8}$$

where n_{s} is the number of stator slots, w_{t} is the width of a stator tooth, r_{s_i} is the stator inner radius, d_{s} is the slot depth, and t_{tt} is the tooth tip thickness. The first term in Eq. (8) accounts for the wire being wrapped around each tooth n_{t} times, while the second term accounts for the end windings.

We next calculate the DC resistance R_{DC} of the windings as

$$R_{\text{DC}} = \frac{\rho(T) l_{\text{w}}}{\pi r_{\text{s}}^2}, \tag{9}$$

where $\rho(T)$ is the temperature-dependent electrical resistivity of the copper windings, and r_{s} is the radius of the conductor winding. We use a linear model for the electrical resistivity, namely

$$\rho(T) = \rho_0 \left(1 + \alpha_\rho \left(T - T_{\rho,0} \right) \right), \tag{10}$$

where ρ_0, α_ρ, and $T_{\rho,0}$ are material-dependent parameters. We take $\rho_0 = 1.678 \times 10^{-8}$ Ωm, $\alpha_\rho = 3.9 \times 10^{-3}$ $\frac{1}{\text{K}}$ and $T_{\rho,0} = 293.15$ K for the copper windings considered in this work. Finally, with the DC resistance calculated, we calculate the DC power loss as

$$P_{\text{DC}} = i^2 R_{\text{DC}}, \tag{11}$$

where i is the root-mean-squared value of the current in the conductor.

The remaining loss terms that we model are the result of time-dependent phenomena. As we have chosen a static approximation to Maxwell's equations, we cannot directly account for these terms in our analysis, and we need to rely on a combination of analytical and empirical methods to model these losses.

We use a hybrid approach to model the AC losses, based on the method presented by Fatemi *et al.* [68]. This approach combines accurate magnetic flux density values from the finite-element solution with an analytical formula for the AC loss in a single strand of wire to efficiently estimate the total AC losses. The AC losses in a single round conductor induced by an externally-oscillating magnetic field can be estimated with the analytical formula [69]

$$p_{\text{AC}} = l \frac{\pi r_{\text{s}}^4 \left(\omega B_{\text{pk}} \right)^2}{\rho(T) \, 8}, \tag{12}$$

where l is the length of the strand exposed to the alternating magnetic field, r_{s} is the strand radius, $\rho(T)$ is the temperature-dependent electrical resistivity, ω is the frequency of oscillation, and B_{pk} is the peak (in time) value of the magnitude of the oscillating magnetic flux density. When we use Eq. (12) to estimate the AC losses of a motor, we take l to be the motor's stack length, and ω to be the angular electrical frequency, related to the motor's RPM S as $\omega = \frac{\pi}{30} n_{\text{p}} S$.

To estimate the value of B_{pk}, we solve Eq. (7) at multiple rotor positions, effectively solving for the magnetic flux density field at different "times". Using all of these field solutions, at each finite element degree of freedom, we estimate the peak (in time) magnetic flux density using the discrete induced exponential smooth max function described by Kennedy and Hicken [70] to obtain the peak magnetic flux density field $\boldsymbol{B}_{pk}^h$. Finally, with this peak magnetic flux density field, we take a homogenized approach and integrate Eq. (12) over the slot area, scaling by the number of strands in the slot, to estimate the total AC losses in the motor, illustrated as

$$P_{AC} = \frac{1}{n_t n_s} \int_{\Omega_W} p_{AC} \, d\Omega_W, \tag{13}$$

where $\Omega_W \subseteq \Omega_E$ is the domain of the motor containing the windings.

We consider the temperature-dependent two-term loss model described by Xue *et al.* [31] to estimate the motor's core losses, defined at a point as

$$p_C = k_h \left(T, f, B_{pk} \right) f B_{pk}^2 + k_e \left(T, f, B_{pk} \right) f^2 B_{pk}^2, \tag{14}$$

where T is the temperature, f is the electrical excitation frequency, and B_{pk} is the magnitude of the peak magnetic flux density. The first term in Eq. (14) represents the core losses caused by hysteresis effects, while the second represents the losses from eddy current effects. The coefficients k_h and k_e are defined through the composition of simple functions and curve-fit data and are described in detail in Appendix B. We use the same procedure described for the AC loss calculation to calculate the B_{pk} field in the stator and rotor needed for the core loss calculation. We integrate Eq. (14) over the stator and rotor to estimate the total core loss across the motor as

$$P_C = \int_{\Omega_S} p_C \, d\Omega_S, \tag{15}$$

where $\Omega_S \subseteq \Omega_E$ is the domain of the motor including the stator and rotor.

We compute the torque, τ, generated by the motor using Coulomb's virtual work method [71, 72] for each of the finite-element field solutions that were used to compute the B_{pk} field. Using these torque values computed at different rotor positions, we compute the average torque produced in the motor, τ_{avg}, and use that to compute the output power produced by the motor as

$$P_{out} = \tau_{avg} S \frac{\pi}{30}. \tag{16}$$

Finally, we compute the motor efficiency, η, as

$$\eta = \frac{P_{out}}{P_{in}}, \tag{17}$$

the fraction of usable power sent to the shaft, P_{out}, divided by the total power provided to the machine $P_{in} = P_{out} + P_{DC} + P_{AC} + P_C$.

D. Thermal Analysis

We model the motor's thermal behavior with the steady-state heat equation, with the divergence of Fourier's law governing thermal diffusion and with source terms added to account for the electromagnetic loss terms. This results in the following linear diffusion equation for the temperature field T:

$$-\nabla \cdot (\mathsf{K}\nabla T) - q_{EM} = 0, \qquad \forall \, \boldsymbol{x} \in \Omega_T. \tag{18}$$

Here, K is the thermal conductivity tensor, and q_{EM} represents the combined heat sources due to the DC, AC, and core losses. The set Ω_T denotes the computational domain of the thermal analysis, taken here to be a two-dimensional cross-section of the motor.

We apply convection boundary conditions to the outside of the motor to account for the cooling provided by air flowing over the outside of the motor's nacelle. This boundary condition is defined such that

$$\mathsf{K}\nabla T \cdot \hat{\boldsymbol{n}} = \mathsf{h} \left(T - T_f \right) \tag{19}$$

along the exterior boundary of Ω_T, where h is the convection heat transfer coefficient, and T_f is the temperature of the fluid flowing outside the boundary. Additionally, we prescribe the Neumann boundary condition

$$\mathsf{K}\nabla T \cdot \hat{\boldsymbol{n}} = q_r \tag{20}$$

along the interior of the rotor to represent the heat transfer from the rotor into the shaft. Specific values used for h, T_{f}, and q_{r} will be specified for each case studied in Section IV.B.

We again use the MFEM library to discretize Eqs. (18), (19), and (20) with the finite element method. This results in the following algebraic form (linear in $\boldsymbol{T}^h$):

$$\boldsymbol{R}_T = \boldsymbol{R}_T(\boldsymbol{T}^h, \boldsymbol{x}^h, \boldsymbol{q}_{\mathrm{EM}}^h, h, T_{\mathrm{f}}, q_{\mathrm{r}}) = \boldsymbol{0}, \tag{21}$$

where $\boldsymbol{T}^h$ is the vector of temperature values at each finite-element degree of freedom, $\boldsymbol{x}^h$ is the vector of mesh node coordinates, and $\boldsymbol{q}_{\mathrm{EM}}^h$ is the vector containing the values of the electromagnetic heat source at each finite-element degree of freedom. We solve Eq. (21) for $\boldsymbol{T}^h$ using the PCG algorithm, again preconditioned with the BoomerAMG preconditioner from the *hypre* library. We use relative and absolute linear solver tolerances of 10^{-12}, and we use the default settings for the BoomerAMG preconditioner in *hypre* version 2.25.0.

With the solution to Eq. (21) obtained, we can compute outputs based on the temperature field. We estimate the maximum steady-state temperature values in each component using the induced exponential smooth max function presented by Kennedy and Hicken [70]. This allows us to place constraints on the temperature field on a component-by-component basis, ensuring that each component (e.g. windings, magnets) does not exceed its maximum allowable temperature, thus avoiding the need to be overly conservative with a single maximum temperature for the entire motor.

III. Coupled Motor Modeling Framework

This section details how we have combined the models presented in Section II into a multi-disciplinary electric motor analysis and optimization framework that considers the coupled electromagnetic and thermal physics of an electric motor. Specifically, we illustrate the coupling between the models used for the forward analysis, and then detail how we efficiently compute derivatives through the coupled model.

We have developed the multi-disciplinary electric motor optimization framework using OpenMDAO [73] by composing several different analysis "components" into a larger analysis. This is represented abstractly by the extended design structure matrix (XDSM) [74] in Fig. 2. In the XDSM, blue ovals represent optimizers; green blocks represent explicit analyses; red blocks represent implicit analyses; orange ovals represent nonlinear solvers; grey parallelograms denote component inputs/outputs that come from/go to other analyses; and white parallelograms denote inputs/outputs provided by/to the user. For the XDSM shown in Fig. 2, the motor's electro-thermal analysis is represented by a generic implicit block, as we consider both feedforward- and feedback-coupled analysis. Such analyses are illustrated by Figs. 3 and 4. Note that in Figs. 3 and 4 the stacks of components associated with the electromagnetic analysis indicate the potentially many solves of Eq. (7) at different rotor positions.

In the feedforward analysis, the electromagnetic analysis does not depend on the computed temperature field, only on an input reference temperature field $\boldsymbol{T}_0^h$. This means that we can sequentially compute each of the analyses shown in the red and green blocks in Fig. 3 without needing any iteration. On the other hand, for the feedback analysis, since both the electromagnetic analysis and the electromagnetic loss calculations depend on the computed temperature field, an implicit system must be converged with a nonlinear solver. We use nonlinear Gauss-Seidel iterations to converge the nonlinear system, with absolute and relative convergence tolerances of 10^{-6}. During the Gauss-Seidel iterations, the electromagnetic and thermal subproblems are solved using their respective solvers; refer to Sections II.C and II.D for the details.

A. Coupled Derivative Computation

We analytically compute derivatives of our model, where possible, to improve the computational efficiency of the optimization. We compute derivatives through the coupled electro-thermal motor analysis using coupled adjoints. To illustrate how we compute the coupled adjoints, we first define the total state vector as the combination of all of the states in the coupled analysis. Considering one solution of Eq. (7) to simplify notation, this is given as

$$\boldsymbol{u} = \begin{bmatrix} \boldsymbol{A}^h \\ \boldsymbol{B}_{\mathrm{pk}}^h \\ \boldsymbol{q}_{\mathrm{EM}}^h \\ \boldsymbol{T}^h \end{bmatrix}. \tag{22}$$
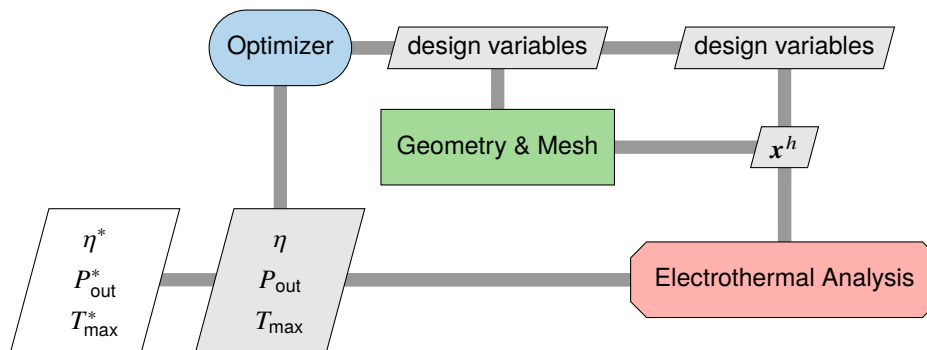
7

Fig. 2 The XDSM for the multi-disciplinary motor optimization shows the data flow considering a generic implicit electro-thermal analysis.
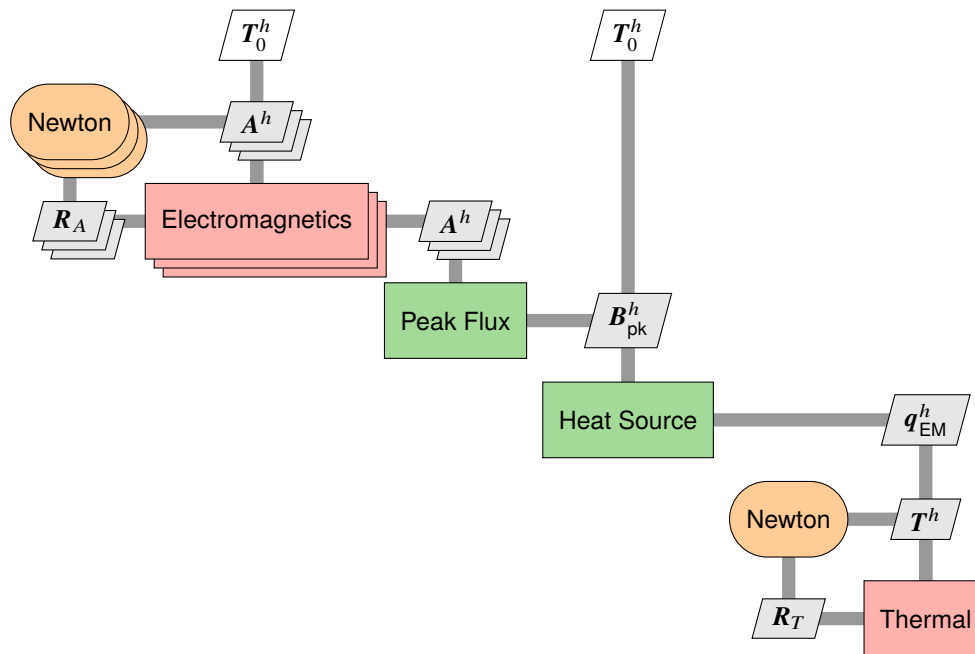

Fig. 3 XDSM for the feedforward coupled electro-thermal analysis, where the electromagnetic analysis depends only on an input reference temperature field T_0^h, not the temperature field computed by the thermal analysis.
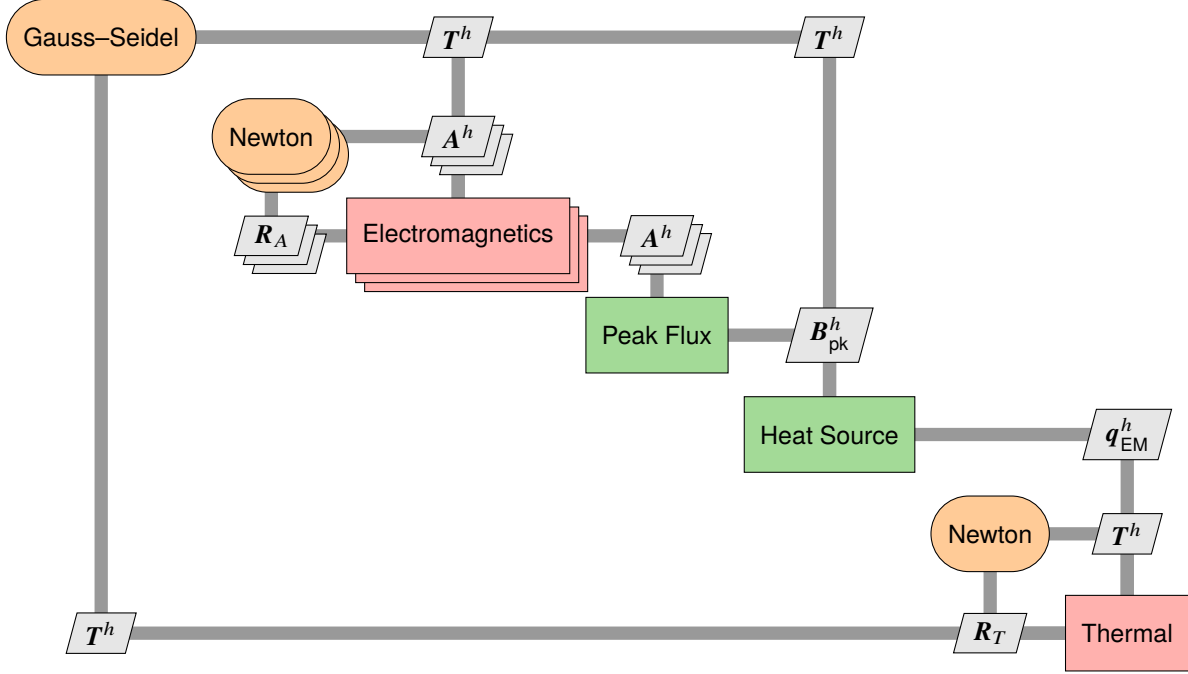
Fig. 4 XDSM for the feedback coupled electro-thermal analysis, where the electromagnetic analysis depends on the temperature field computed by the thermal analysis, and the implicit system must be converged by a solver.

Next, we define the residual of the coupled model as the combination of all the individual residuals,

$$
\boldsymbol{R}(\boldsymbol{u}) = \begin{bmatrix} \boldsymbol{R}_A \\ \hat{\boldsymbol{B}}_{\text{pk}}^h - \boldsymbol{B}_{\text{pk}}^h \\ \hat{\boldsymbol{q}}_{\text{EM}}^h - \boldsymbol{q}_{\text{EM}}^h \\ \boldsymbol{R}_T \end{bmatrix}, \tag{23}
$$

where we have made an implicit transformation of the explicit functions that compute $\boldsymbol{B}_{\text{pk}}^h$ and $\boldsymbol{q}_{\text{EM}}^h$. Note that we have dropped explicit functional dependencies in the residuals, $\boldsymbol{R}_A$ and $\boldsymbol{R}_T$, to simplify notation. Considering a generic motor output f for illustration, the coupled adjoint system is given as

$$
\begin{bmatrix} \frac{\partial \boldsymbol{R}_A}{\partial \boldsymbol{A}^h} & \boldsymbol{0} & \boldsymbol{0} & \frac{\partial \boldsymbol{R}_A}{\partial \boldsymbol{T}^h} \\ -\frac{\partial \boldsymbol{B}_{\text{pk}}^h}{\partial \boldsymbol{A}^h} & -\mathrm{I} & \boldsymbol{0} & \boldsymbol{0} \\ \boldsymbol{0} & -\frac{\partial \boldsymbol{q}_{\text{EM}}^h}{\partial \boldsymbol{B}_{\text{pk}}^h} & -\mathrm{I} & -\frac{\partial \boldsymbol{q}_{\text{EM}}^h}{\partial \boldsymbol{T}^h} \\ \boldsymbol{0} & \boldsymbol{0} & \frac{\partial \boldsymbol{R}_T}{\partial \boldsymbol{q}_{\text{EM}}^h} & \frac{\partial \boldsymbol{R}_T}{\partial \boldsymbol{T}^h} \end{bmatrix}^{\mathrm{T}} \begin{bmatrix} \boldsymbol{\psi}_A \\ \boldsymbol{\psi}_{B_{\text{pk}}} \\ \boldsymbol{\psi}_{q_{\text{EM}}} \\ \boldsymbol{\psi}_T \end{bmatrix} = - \begin{bmatrix} \frac{\partial f}{\partial \boldsymbol{A}^h}^{\mathrm{T}} \\ \frac{\partial f}{\partial \boldsymbol{B}_{\text{pk}}^h}^{\mathrm{T}} \\ \frac{\partial f}{\partial \boldsymbol{q}_{\text{EM}}^h}^{\mathrm{T}} \\ \frac{\partial f}{\partial \boldsymbol{T}^h}^{\mathrm{T}} \end{bmatrix}. \tag{24}
$$

Each partial derivative term in Eq. (24) is analytically computed using a combination of hand-coded and operator-overloading-based algorithmic differentiation [75].

We solve the linear system in Eq. (24) using the Generalized Minimal RESidual (GMRES) method [76], preconditioned with two iterations of linear block Gauss-Seidel (LBGS). The block Gauss-Seidel preconditioner allows us to re-use the single-discipline specific adjoint solvers that have been developed for each discipline. We solve for each of the single-discipline adjoints during the LBGS iteration using PCG, preconditioned with the same AMG preconditioners used in each discipline's forward problem. We use relative and absolute linear solver tolerances of 10^{-12} when computing the single-discipline adjoint solutions. We use relative and absolute linear solver tolerances of 10^{-6} for the coupled GMRES adjoint solution.* In the case of the feedforward analysis, the terms above the diagonal in

---

*The authors note that careful attention must be paid to the relative scaling of the terms in Eq. (23) in order to ensure that the iterative solution of Eq. (24) converges tightly.
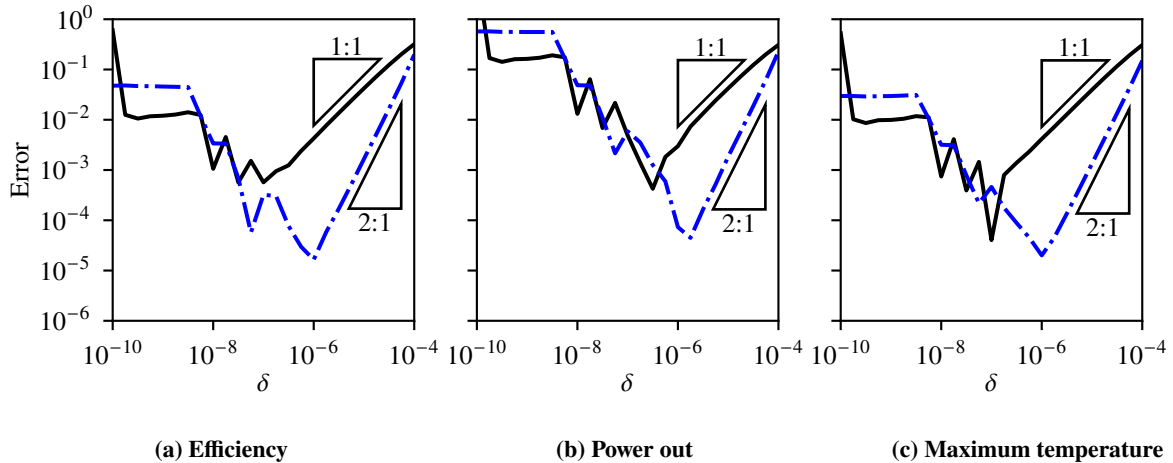
9

Fig. 5 **The error in the finite-difference directional-derivative approximations converge with decreasing step size at the expected rate before becoming inaccurate due to subtractive cancellation. The first-order forward difference is shown in solid black, while the second-order central difference is shown in dot-dashed blue.**

the (non-transposed) system matrix in Eq. (24) are zero. In this case, the adjoint system can be efficiently solved directly using block back-substitution, which is equivalent to applying one iteration of LBGS.

We rely on OpenMDAO [73] to assemble the linear system defined in Eq. (24) for each of the functions of interest for our optimization, and to then compute the required total derivatives of each function using the unified derivatives equations (UDE) [77, 78]. We provide analytically differentiated partial derivatives for each term in the analysis that we are able to. Unfortunately, we are unable to analytically differentiate through the ESP CAD system, so we rely on finite differences to compute the required derivatives. We use forward-difference finite differences with step size $\delta = 10^{-6}$ to compute the partial derivatives of the mesh coordinates x^h with respect to the geometric design variables identified in Table 1.

IV. Results and Discussion

In this section, we present a verification study of the analytical derivatives we compute through the electro-thermal analysis and then present a series of optimization results. Specifically, we consider two optimizations using the feedforward-coupled model, each using a different reference temperature, and an additional optimization using the feedback-coupled model.

A. Derivative Verification

We verify the accuracy of our analytically computed derivatives by comparing them to both a forward and central finite-difference directional derivative. We analytically compute a directional derivative of the efficiency, power out, and maximum temperature outputs with respect to all of the motor's design variables in a normalized random perturbation direction. Then, using the same perturbation direction, we compute a series of first-order forward- and second-order central-difference finite-difference derivative approximations, sweeping from finite difference step size $\delta = 10^{-4}$ to 10^{-10}. Finally, we plot the absolute value of the relative error in the finite-difference derivative approximations on a log-log scale in Figure 5. As expected, the forward difference error converges as $O(\delta)$, while the central difference error converges as $O(\delta^2)$. The finite-difference derivative approximations eventually become inaccurate as floating point errors due to subtractive cancellation begin to dominate. The agreement that we do see between the analytically computed derivatives and the finite differences gives us confidence that the analytical derivatives are correct.

B. Optimization Results

With the model derivatives verified, we now describe the optimization problem we use to demonstrate the use of the analytically computed derivatives through the coupled model. The objective of the optimization is to maximize the

Table 3 Electric-motor optimization problem statement.

	Function/variable			Description
maximize		η		Motor efficiency
with respect to	10 mm $\leq$	l_s	$\leq$ 80 mm	Stack length
	1 mm $\leq$	d_s		Slot depth
	1 mm $\leq$	t_m	$\leq$ 5 mm	Magnet thickness
	10 mm $\leq$	r_{r_i}		Rotor inner radius
		r_{r_o}		Rotor outer radius
		r_{s_i}		Stator inner radius
		r_{s_o}	$\leq$ 100 mm	Stator outer radius
	2.5 mm $\leq$	w_t		Tooth width
	0.75 mm $\leq$	t_tt		Tooth tip thickness
	0.1 mm $\leq$	r_s	$\leq$ 0.32 mm	Strand radius
	1.75 A $<$	i		Strand RMS current
	10 $\leq$	n_t		Number of turns
subject to	P_out = 10 kW			Output power
	T_max = 413.15 K			Motor maximum temperature
	$t_\text{ry} \equiv r_{\text{r}_\text{o}} - r_{\text{r}_\text{i}} \geq$ 1 mm			Rotor yoke thickness
	$t_\text{sy} \equiv r_{\text{s}_\text{o}} - r_{\text{s}_\text{i}} - d_\text{s} \geq$ 1 mm			Stator yoke thickness
	$t_\text{g} \equiv r_{\text{s}_\text{i}} - r_{\text{r}_\text{o}} - t_\text{m} =$ 1 mm			Air-gap thickness

efficiency of the motor, subject to power out, thermal, and geometric constraints. Table 3 provides a summary of the optimization problem. In lieu of a model that estimates the voltage required by the motor, we artificially put lower bounds on the current and stack length design variables. The authors have found that without imposing a constraint on these design variables during optimizations, the optimizer will tend to increase the stack length and reduce the current to such low levels that the resulting design would require motor drives capable of producing unreasonably high voltages to meet the motor's output power requirement. We solve the optimization problem given in Table 3 using both the feedforward- and feedback-coupled models described in Section III; we adopt reference temperatures of $T_0 = 333.15$ K and $T_0 = 373.15$ K for the two feedforward problems.

We start each optimization from the initial design specified in Table 4, with the remaining fixed parameters given in Table 5. The initial motor geometries and their corresponding magnetic flux-density fields are plotted in Fig. 6. We use SNOPT [79, 80] version 7.7.1 with optimality and feasibility tolerances of 10^{-6} to solve the electric motor optimization problems. We interface with SNOPT using OpenMDAO [73] through the PyOptSparse [81] optimization driver.

We plot the optimized geometries and magnetic flux density fields for each optimization in Fig. 7, and the optimization optimality and feasibility histories in Fig. 8. While not every case was able to achieve the optimality tolerance of 10^{-6}, each was able to reduce the norm in the optimality by at least 5 orders of magnitude, indicating strong convergence. In each case, the final feasibility achieved was below the desired tolerance.

Each optimization case successfully improved the motor efficiency compared to the infeasible initial design, while simultaneously satisfying all constraints. The optimization of the feedback-coupled model raised the efficiency from 95.6 % to 98.0 %, while the feedforward-coupled models raised the efficiency from 95.9 % and 95.8 %, to 98.2 % and 98.1 %, for the $T_0 = 333.15$ K and $T_0 = 373.15$ K cases, respectively. Further, the maximum motor temperature computed by the feedback-coupled model at its optimized design is 390.0 K. The maximum motor temperatures at the ends of the feedforward-coupled optimizations are 383.2 K and 390.0 K for the $T_0 = 333.15$ K and $T_0 = 373.15$ K cases, respectively.

At first glance, it may be surprising that the feedforward-coupled optimized designs seem more performant than the feedback-coupled optimized design; the optimized feed-forward efficiencies given in Table 4 are higher than the
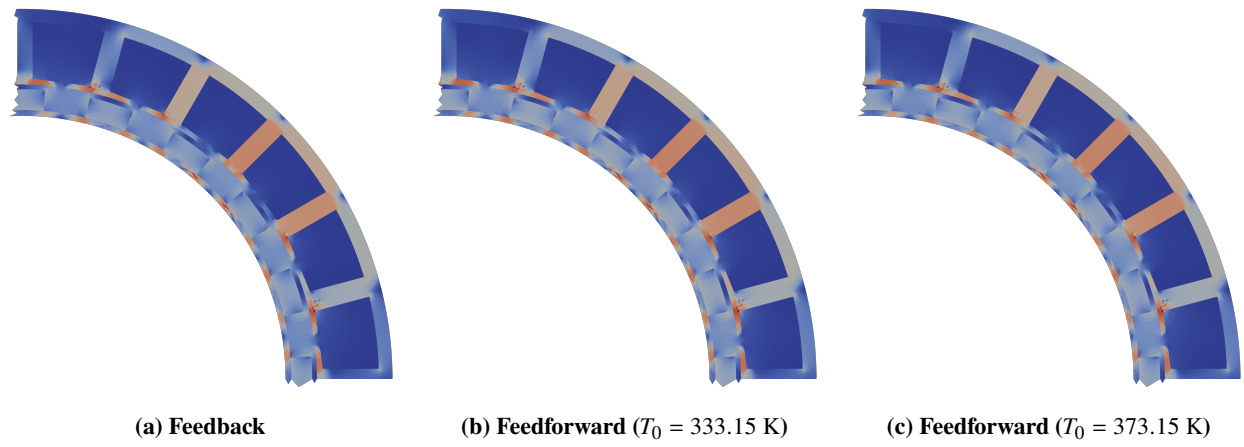
(a) Feedback   (b) Feedforward ($T_0 = 333.15$ K)   (c) Feedforward ($T_0 = 373.15$ K)

Fig. 6   **The magnitude of the magnetic flux density in the different initial motor geometries. Note that while only a quarter of the geometry is shown, the full motor was simulated.**
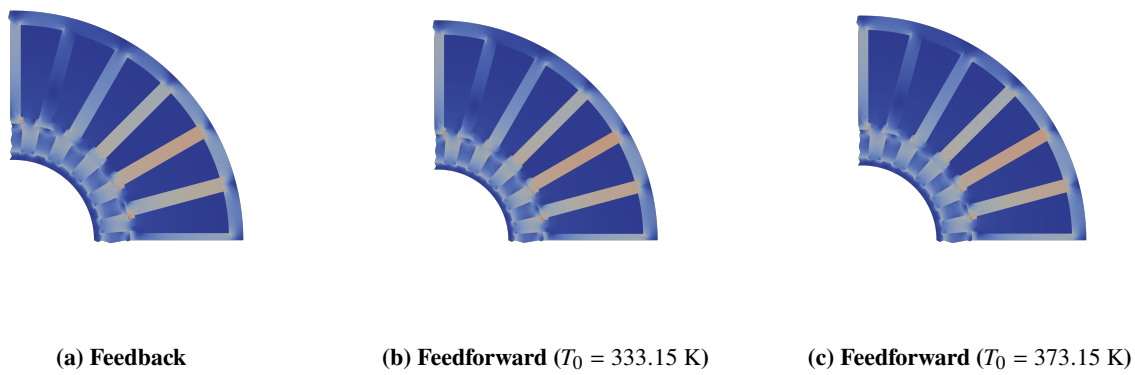

(a) Feedback   (b) Feedforward ($T_0 = 333.15$ K)   (c) Feedforward ($T_0 = 373.15$ K)

Fig. 7   **The magnitude of the magnetic flux density in the different optimized motor geometries. Note that while only a quarter of the geometry is shown, the full motor was simulated. The optimized geometries are plotted on the same scale as the initial geometries shown in Fig. 6.**

Table 4 Electric-motor design variables and outputs for the initial design and optimized designs.

	Initial Design	Feedback	Feedforward $T_0 = 333.15$ K	$T_0 = 373.15$ K
η	-	97.995 %	98.223 %	98.059 %
η_0	-	95.557 %	95.932 %	95.775 %
l_s	34.5 mm	80.0 mm	80.0 mm	80.0 mm
d_s	12.1 mm	19.401 mm	19.613 mm	19.638 mm
t_m	4.4 mm	5.0 mm	5.0 mm	5.0 mm
r_{r_i}	55.625 mm	17.000 mm	14.960 mm	15.834 mm
r_{r_o}	61.250 mm	23.641 mm	21.380 mm	22.350 mm
r_{s_i}	62.250 mm	24.641 mm	22.380 mm	23.350 mm
r_{s_o}	78.225 mm	48.542 mm	46.492 mm	47.488 mm
w_t	4.3 mm	3.059 mm	2.728 mm	2.809 mm
t_tt	1.0 mm	1.5 mm	1.5 mm	1.5 mm
r_s	0.32 mm	0.32 mm	0.32 mm	0.32 mm
i	2.0 A	1.75 A	1.75 A	1.75 A
n_t	100	85.286	83.006	85.611
P_out	-	10.000 kW	10.000 kW	10.000 kW
$P_{\text{out},0}$	-	4.256 kW	4.342 kW	4.319 kW
T_max	-	389.990 K	383.217 K	389.569 K
$T_{\text{max},0}$	-	420.469 K	410.990 K	415.311 K
t_ry	1.225 mm	1.642 mm	1.419 mm	1.516 mm
t_sy	2.875 mm	3.0 mm	3.0 mm	3.0 mm
t_g	1.0 mm	1.0 mm	1.0 mm	1.0 mm

Table 5 Electric-motor optimization fixed parameters.

Parameter	Value
S	6000 RPM
n_p	20
n_s	24
h	$100 \ \frac{\text{W}}{\text{m}^2\text{K}}$
T_f	293.15 K
q_r	$10 \ \frac{\text{W}}{\text{m}^2}$

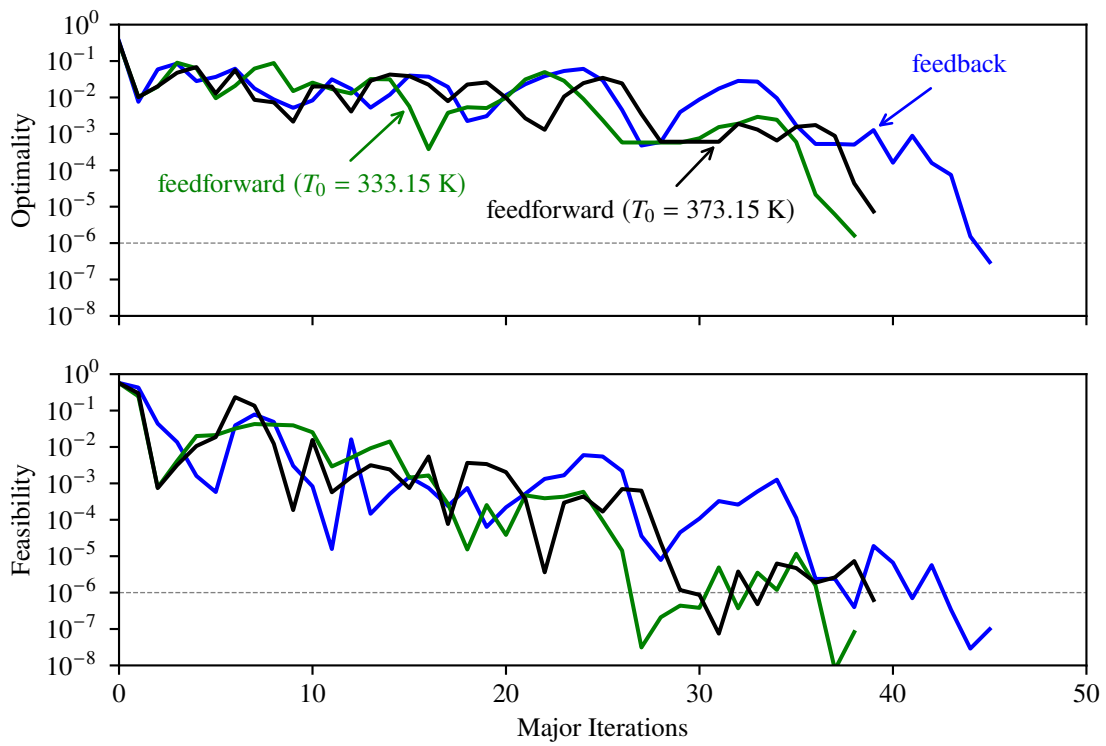**Fig. 8** **Convergence history for the coupled electric motor optimization problem defined in Table 3, considering both feedback and feedforward coupled models.**

feedback efficiency, and the maximum motor temperatures are lower than the feedback maximum temperature. However, the results reported in Table 4 are accurate according to the model that was used to compute them. Running the feedback-coupled model on the feedforward-optimized designs reveals that under the higher-fidelity feedback-coupled model, the feedforward-optimized design would not produce the required output power, producing only 9.378 kW for the $T_0 = 333.15$ K case, and 9.793 kW for the $T_0 = 373.15$ K case.

Since the feedforward-coupled model does not update the temperature during the optimization, it does not adequately model the effects of temperature on the magnetic field solution if the reference temperature is far from the true temperature. For the $T_0 = 333.15$ K case, the feedback-coupled model computes a maximum temperature of 388 K. This 55 K temperature difference between the feedback- and feedforward-coupled models accounts for the 622 W difference in output power between the models for the same design. This discrepancy between the feedforward- and feedback-coupled models motivates the need for feedback coupling, particularly for optimizations where it is unlikely that a known temperature distribution can be assumed a priori.

V. Conclusions

Numerical optimization of electric motors will increasingly become a critical component of the design of new electrified aircraft. This paper has presented a coupled electro-thermal multi-disciplinary motor analysis and optimization framework. We have used coupled adjoints to analytically differentiate through the coupled analysis, enabling the use of scalable gradient-based optimization algorithms.

We subsequently demonstrated the optimization framework on a series of realistic aerospace-grade electric motor optimization problems. We conducted optimizations considering both feedforward- and feedback-coupled analysis models. Further, we showed that the feedforward-coupled optimized designs are infeasible when analyzed by the feedback-coupled analysis, further motivating the need for feedback-coupled modeling.

Future work is needed to further increase the fidelity of the coupled model, particularly the inclusion of a model for the heat transfer due to the turbulent Taylor-Couette flow in the motor's air gap, and a more sophisticated demagnetization model. Further, validation of the model against experimental data is needed to prove its merit and predictive capabilities. Nevertheless, no matter the model, the use of coupled adjoints will allow efficient gradient-based optimization of electric motors at whichever phase of the design process an engineer desires.

Appendix

A. Reluctivity Model

We model the reluctivity, $\nu(\boldsymbol{B})$, as a piecewise-continuous function $\nu : \mathbb{R} \to \mathbb{R}$, $\forall \, \boldsymbol{x} \in \Omega_{\mathrm{E}}$, where each sub-function of ν is based on the material it is in. We use constant values for the reluctivity in the motor's air gap, magnets and windings. For the air gap and motor windings this value is the reluctivity of free space $\nu_0 = \frac{1}{\mu_0} = \frac{1}{4\pi \times 10^{-7}}$. For the magnets, we use the constant value $\nu_{\mathrm{mag}} = \frac{1}{\mu_{\mathrm{r}}\mu_0}$, where μ_{r} is the magnet's relative permeability, a value commonly listed in a material datasheet. We use a value of $\mu_{\mathrm{r}} = 1.04$ for the $\mathrm{Nd_2Fe_{14}B}$ magnets considered in this work.

The reluctivity of the motor's steel (the material used in the stator and rotor) is more complicated than the rest of the components as it is a nonlinear function of the magnetic flux density. The model used is written as

$$\nu_{\mathrm{Fe}} = \exp\left(f\left(\|\boldsymbol{B}\|\right)\right), \tag{25}$$

where $f(\|\boldsymbol{B}\|)$ is a cubic B-spline that represents the log-transformed reluctivity as a function of the magnitude of the magnetic flux density. The B-spline knot vector and control points are found by minimizing the least-squares error between the spline and discrete B-ν data points. The control points and knot vector for the Hiperco 50 magnetic steel used for the results presented in this work are listed in Table 6. Thus, the final reluctivity function is given as

$$\nu(\boldsymbol{B}) = \begin{cases} \frac{1}{\mu_0} & \boldsymbol{x} \in \Omega_{\mathrm{air}} \\ \frac{1}{\mu_0} & \boldsymbol{x} \in \Omega_{\mathrm{W}} \\ \frac{1}{\mu_{\mathrm{r}}\mu_0} & \boldsymbol{x} \in \Omega_{\mathrm{mag}} \\ \nu_{\mathrm{Fe}}\left(\|\boldsymbol{B}\|\right) & \boldsymbol{x} \in \Omega_{\mathrm{S}} \end{cases}. \tag{26}$$

Table 6 Control points and knot vector for the cubic B-spline fit used in the Hiperco 50 reluctivity calculation.

Control Points	Knots
5.5286	0.0
5.4645	0.0
4.5597	0.0
4.2891	0.0
3.8445	0.1479
4.2880	0.5757
4.9505	0.9924
11.9364	1.4090
11.9738	1.8257
12.6554	2.2424
12.8097	2.6590
13.3347	3.0757
13.5871	3.4924
13.5871	3.9114
13.5871	8.0039
	10.0
	10.0
	10.0
	10.0

B. Core Loss Model

We follow Xue *et al.* [31] and define the core loss coefficient functions k_h and k_e as

$$k_h(T, f, B_{pk}) = k_{th}(T, f, B_{pk})k_{h,T_{C,0}}(f, B_{pk}), \tag{27}$$

and

$$k_e(T, f, B_{pk}) = k_{te}(T, f, B_{pk})k_{e,T_{C,0}}(f, B_{pk}), \tag{28}$$

where k_{th} and k_{te} are the temperature-dependent hysteresis and eddy-current coefficients, and $k_{h,T_{C,0}}$ and $k_{e,T_{C,0}}$ are the coefficients defined at the reference temperature $T_{C,0}$. We define k_{th} and k_{te} as

$$k_{th}(T, f, B_{pk}) = 1 + (T - T_{C,0})D_h(f, B_{pk}), \tag{29}$$

and

$$k_{te}(T, f, B_{pk}) = 1 + (T - T_{C,0})D_e(f, B_{pk}), \tag{30}$$

where we further define $D_h(f, B_{pk})$ and $D_e(f, B_{pk})$ as

$$D_h(f, B_{pk}) = \frac{k_{h,T_{C,1}}(f, B_{pk}) - k_{h,T_{C,0}}(f, B_{pk})}{(T_{C,1} - T_{C,0})k_{h,T_{C,0}}(f, B_{pk})}, \tag{31}$$

and

$$D_e(f, B_{pk}) = \frac{k_{e,T_{C,1}}(f, B_{pk}) - k_{e,T_{C,0}}(f, B_{pk})}{(T_{C,1} - T_{C,0})k_{e,T_{C,0}}(f, B_{pk})}. \tag{32}$$

Here $k_{h,T_{C,1}}(f, B_{pk})$, $k_{h,T_{C,0}}(f, B_{pk})$, $k_{e,T_{C,1}}(f, B_{pk})$, and $k_{e,T_{C,0}}(f, B_{pk})$ are the hysteresis and eddy-current loss coefficient functions at the reference temperatures $T_{C,1}$ and $T_{C,0}$ respectively.

Table 7 Empirical hysteresis and eddy-current coefficients used for the core loss models computed using data from [82].

	k_{h_0}	k_{h_1}	k_{h_2}	k_{h_3}
$T_{C,0} = 296.15$ K	5.978×10^{-2}	-6.586×10^{-2}	3.521×10^{-2}	-6.548×10^{-3}
$T_{C,1} = 423.15$ K	5.787×10^{-2}	-7.947×10^{-2}	5.092×10^{-2}	-1.111×10^{-2}
	k_{e_0}	k_{e_1}	k_{e_2}	k_{e_3}
$T_{C,0} = 296.15$ K	3.831×10^{-5}	-4.200×10^{-5}	2.098×10^{-5}	-3.886×10^{-6}
$T_{C,1} = 423.15$ K	3.205×10^{-5}	-1.435×10^{-5}	-3.748×10^{-6}	2.685×10^{-6}

We use third-order polynomials to model these coefficient functions. For each of the two reference temperatures, the forms of these polynomials are respectively given as

$$k_{h,T_C}(f, B_{pk}) = k_{h_0} + k_{h_1} B_{pk} + k_{h_2} B_{pk}^2 + k_{h_3} B_{pk}^3, \tag{33}$$

and

$$k_{e,T_C}(f, B_{pk}) = k_{e_0} + k_{e_1} B_{pk} + k_{e_2} B_{pk}^2 + k_{e_3} B_{pk}^3. \tag{34}$$

We use tabulated experimental Supermendur core loss data from Wieserman *et al.* [82] for the determination of empirical parameters in the temperature-dependent core loss model. Using this experimental data, we perform a linear least-squares curve fit across a spectrum of frequencies to yield the hysteresis and eddy current coefficients shown in Table 7.

Acknowledgments

References

[1] Lukic, M., Giangrande, P., Hebala, A., Nuzzo, S., and Galea, M., "Review, challenges, and future developments of electric taxiing systems," *IEEE Transactions on Transportation Electrification*, Vol. 5, No. 4, 2019, pp. 1441–1457.

[2] Lee, D., Fahey, D., Skowron, A., Allen, M., Burkhardt, U., Chen, Q., Doherty, S., Freeman, S., Forster, P., Fuglestvedt, J., Gettelman, A., De León, R., Lim, L., Lund, M., Millar, R., Owen, B., Penner, J., Pitari, G., Prather, M., Sausen, R., and Wilcox, L., "The contribution of global aviation to anthropogenic climate forcing for 2000 to 2018," *Atmospheric Environment*, Vol. 244, 2021, p. 117834. https://doi.org/https://doi.org/10.1016/j.atmosenv.2020.117834.

[3] Schäfer, A. W., Barrett, S. R., Doyme, K., Dray, L. M., Gnadt, A. R., Self, R., O'Sullivan, A., Synodinos, A. P., and Torija, A. J., "Technological, economic and environmental prospects of all-electric aircraft," *Nature Energy*, Vol. 4, No. 2, 2019, pp. 160–166.

[4] Lee, D. S., Fahey, D. W., Forster, P. M., Newton, P. J., Wit, R. C., Lim, L. L., Owen, B., and Sausen, R., "Aviation and global climate change in the 21st century," *Atmospheric environment*, Vol. 43, No. 22-23, 2009, pp. 3520–3537.

[5] Dorbian, C. S., Wolfe, P. J., and Waitz, I. A., "Estimating the climate and air quality benefits of aviation fuel and emissions reductions," *Atmospheric Environment*, Vol. 45, No. 16, 2011, pp. 2750–2759.

[6] Yim, S. H., Lee, G. L., Lee, I. H., Allroggen, F., Ashok, A., Caiazzo, F., Eastham, S. D., Malina, R., and Barrett, S. R., "Global, regional and local health impacts of civil aviation emissions," *Environmental Research Letters*, Vol. 10, No. 3, 2015, p. 034001.

[7] Sarlioglu, B., and Morris, C. T., "More electric aircraft: Review, challenges, and opportunities for commercial transport aircraft," *IEEE transactions on Transportation Electrification*, Vol. 1, No. 1, 2015, pp. 54–64. https://doi.org/https://doi.org/10.1109/TTE.2015.2426499.

[8] Viswanathan, V., Epstein, A. H., Chiang, Y.-M., Takeuchi, E., Bradley, M., Langford, J., and Winter, M., "The challenges and opportunities of battery-powered flight," *Nature*, Vol. 601, No. 7894, 2022, pp. 519–525.

[9] Brelje, B. J., and Martins, J. R., "Electric, hybrid, and turboelectric fixed-wing aircraft: A review of concepts, models, and design approaches," *Progress in Aerospace Sciences*, Vol. 104, 2019, pp. 1–19. https://doi.org/10.1016/j.paerosci.2018.06.004.

[10] Follen, G. J., Del Rosario, R., Wahls, R., and Madavan, N., "NASA's fundamental aeronautics subsonic fixed wing project: generation n+ 3 technology portfolio," Tech. rep., SAE Technical Paper, 2011.

[11] Falck, R. D., Chin, J., Schnulo, S. L., Burt, J. M., and Gray, J. S., "Trajectory optimization of electric aircraft subject to subsystem thermal constraints," *18th AIAA/ISSMO Multidisciplinary Analysis and Optimization Conference*, 2017, p. 4002.

[12] Ansys, "Ansys Motor-CAD — Electric Motor Design Software," Ansys Website: https://www.ansys.com/products/electronics/ansys-motor-cad, 2023. Accessed: 05/3/2023.

[13] Ansys, "Ansys Maxwell | Electromechanical Device Analysis Software," Ansys Website: https://www.ansys.com/products/electronics/ansys-maxwell, 2023. Accessed: 05/3/2023.

[14] Altair, "Accelerate Motor, Sensor, and Actuator Design | Altair Flux," Altair Website: https://www.altair.com/flux, 2023. Accessed: 05/3/2023.

[15] Altair, "Electric Rotating Motor Design | FluxMotor," Altair Website: https://www.altair.com/fluxmotor, 2023. Accessed: 05/3/2023.

[16] Ruoho, S., Dlala, E., and Arkkio, A., "Comparison of Demagnetization Models for Finite-Element Analysis of Permanent-Magnet Synchronous Machines," *IEEE Transactions on Magnetics*, Vol. 43, No. 11, 2007, pp. 3964–3968. https://doi.org/10.1109/TMAG.2007.906749.

[17] Kral, C., Sprangers, R., Waarma, J., Haumer, A., Winter, O., and Lomonova, E., "Modeling Demagnetization Effects in Permanent Magnet Synchronous Machines," *The XIX International Conference on Electrical Machines-ICEM 2010*, IEEE, Rome, Italy, September 2010, pp. 1–6. https://doi.org/10.1109/ICELMACH.2010.5608315.

[18] Hamidizadeh, S., Alatawneh, N., Chromik, R. R., and Lowther, D. A., "Comparison of different demagnetization models of permanent magnet in machines for electric vehicle application," *IEEE Transactions on Magnetics*, Vol. 52, No. 5, 2016, pp. 1–4.

[19] Ruoho, S., "Modeling Demagnetization of Sintered NdFeB Magnet Material in Time-Discretized Finite Element Analysis," Ph.D. thesis, Department of Electrical Engineering, Aalto University, Espoo, Finland, January 2011.

[20] Sjökvist, S., and Eriksson, S., "Experimental Verification of a Simulation Model for Partial Demagnetization of Permanent Magnets," *IEEE Transactions on Magnetics*, Vol. 50, No. 12, 2014, pp. 1–5. https://doi.org/10.1109/TMAG.2014.2339795.

[21] Zhou, P., Lin, D., Xiao, Y., Lambert, N., and Rahman, M. A., "Temperature-Dependent Demagnetization Model of Permanent Magnets for Finite Element Analysis," *IEEE Transactions on Magnetics*, Vol. 48, No. 2, 2012, pp. 1031–1034. https://doi.org/10.1109/TMAG.2011.2172395.

[22] Kern, A., Leuning, N., and Hameyer, K., "Semi-Physical Demagnetization Model for the Temperature Dependency of Permanent Magnets in Electrical Machines," *AIP Advances*, Vol. 13, No. 2, 2023, p. 025105. https://doi.org/10.1063/9.0000400.

[23] Krings, A., "Iron losses in electrical machines-influence of material properties, manufacturing processes, and inverter operation," Ph.D. thesis, KTH Royal Institute of Technology, 2014.

[24] Boglietti, A., Cavagnino, A., Lazzari, M., and Pastorelli, M., "Predicting Iron Losses in Soft Magnetic Materials With Arbitrary Voltage Supply: An Engineering Approach," *IEEE Transactions on Magnetics*, Vol. 39, No. 2, 2003, pp. 981–989. https://doi.org/10.1109/TMAG.2003.808599.

[25] Magnussen, F., "On Design and Analysis of Synchronous Permanent Magnet Machines for Field-Weakening Operation in Hybrid Electric Vehicles," Ph.D. thesis, Department of Electrical Engineering, KTH Royal Institute of Technology, Stockholm, Sweden, 2004.

[26] Tsai, W.-C., "Effects of Core Materials and Operating Parameters on Core Losses in a Brushless DC Motor," *International Journal of Engineering and Industries*, Vol. 2, No. 1, March 2011, pp. 51–61. https://doi.org/10.4156/ijei.vol2.issue1.7.

[27] Huang, X., Goodman, A., Gerada, C., Fang, Y., and Lu, Q., "Design of a Five-Phase Brushless DC Motor for a Safety Critical Aerospace Application," *IEEE Transactions on Industrial Electronics*, Vol. 59, No. 9, 2012, pp. 3532–3541. https://doi.org/10.1109/TIE.2011.2172170.

[28] Zou, J., Qi, W., Xu, Y., Xu, F., Li, Y., and Li, J., "Design of Deep Sea Oil-Filled Brushless DC Motors Considering the High Pressure Effect," *IEEE Transactions on Magnetics*, Vol. 48, No. 11, 2012, pp. 4220–4223. https://doi.org/10.1109/TMAG.2012.2204731.

[29] Miyamasu, M., and Akatsu, K., "Efficiency Comparison Between Brushless DC Motor and Brushless AC Motor Considering Driving Method and Machine Design," *IEEJ Journal of Industry Applications*, Vol. 2, No. 1, 2013, pp. 79–86. https://doi.org/10.1541/ieejjia.2.79.

[30] Ivan Maradzhiev, E. D., Tsvetana Grigorova, "Investigation of Power Losses by Various Brushless Motor Modulation Methods in Motor Mode," *Universal Journal of Electrical and Electronic Engineering*, Vol. 7, No. 2, 2020, pp. 88–93. https://doi.org/10.13189/ujeee.2020.070203.

[31] Xue, S., Feng, J., Guo, S., Peng, J., Chu, W., and Zhu, Z., "A new iron loss model for temperature dependencies of hysteresis and eddy current losses in electrical machines," *IEEE Transactions on Magnetics*, Vol. 54, No. 1, 2017, pp. 1–10.

[32] Zhu, Z.-Q., Xue, S., Chu, W., Feng, J., Guo, S., Chen, Z., and Peng, J., "Evaluation of Iron Loss Models in Electrical Machines," *IEEE Transactions on Industry Applications*, Vol. 55, No. 2, 2019, pp. 1461–1472. https://doi.org/10.1109/TIA.2018.2880674.

[33] Jiang, W., and Jahns, T. M., "Coupled Electromagnetic–Thermal Analysis of Electric Machines Including Transient Operation Based on Finite-Element Techniques," *IEEE Transactions on Industry Applications*, Vol. 51, No. 2, 2015, pp. 1880–1889. https://doi.org/10.1109/TIA.2014.2345955.

[34] Chen, X., Wang, J., and Griffo, A., "A High-Fidelity and Computationally Efficient Electrothermally Coupled Model for Interior Permanent-Magnet Machines in Electric Vehicle Traction Applications," *IEEE Transactions on Transportation Electrification*, Vol. 1, No. 4, 2015, pp. 336–347. https://doi.org/10.1109/TTE.2015.2478257.

[35] Tong, W., Sun, R., Li, S., and Tang, R., "Loss and Thermal Analysis for High-Speed Amorphous Metal PMSMs Using 3-D Electromagnetic-thermal Bi-Directional Coupling," *IEEE Transactions on Energy Conversion*, Vol. 36, No. 4, 2021, pp. 2839–2849. https://doi.org/10.1109/TEC.2021.3065336.

[36] Yu, W., Hua, W., Qi, J., Zhang, H., Zhang, G., Xiao, H., Xu, S., and Ma, G., "Coupled Magnetic Field-Thermal Network Analysis of Modular-Spoke-Type Permanent-Magnet Machine for Electric Motorcycle," *IEEE Transactions on Energy Conversion*, Vol. 36, No. 1, 2021, pp. 120–130. https://doi.org/10.1109/TEC.2020.3006098.

[37] Bianchi, N., and Bolognani, S., "Brushless dc motor design: an optimisation procedure based on genetic algorithms," 1997.

[38] Hwang, C., and Chang, J., "Design and analysis of a high power density and high efficiency permanent magnet DC motor," *Journal of Magnetism and Magnetic Materials*, Vol. 209, No. 1-3, 2000, pp. 234–236.

[39] Upadhyay, P., and Rajagopal, K., "Genetic algorithm based design optimization of a permanent magnet brushless dc motor," *Journal of Applied Physics*, Vol. 97, No. 10, 2005, p. 10Q516.

[40] You, Y.-M., and Chung, D.-W., "Optimal Design of a Permanent Magnet Synchronous Motor To Improve Torque and Demagnetization Characteristics," *J. Magn.*, Vol. 22, No. 3, 2017, pp. 423–429. https://doi.org/10.4283/JMAG.2017.22.3.423.

[41] You, Y.-m., and Yoon, K.-y., "Multi-Objective Optimization of Permanent Magnet Synchronous Motor for Electric Vehicle Considering Demagnetization," *Applied Sciences*, Vol. 11, No. 5, 2021, p. 2159. https://doi.org/10.3390/app11052159.

[42] Golovanov, D., Gerada, D., Xu, Z., Gerada, C., Page, A., and Sawata, T., "Designing an Advanced Electrical Motor for Propulsion of Electric Aircraft," *AIAA Propulsion and Energy 2019 Forum*, AIAA 2019-4482, Indianapolis, IN, August 2019. https://doi.org/10.2514/6.2019-4482.

[43] Wang, M., Zhu, H., Zhou, C., Zheng, P., and Tong, C., "Analysis and Optimization of a V-Shape Combined Pole Interior Permanent-Magnet Synchronous Machine With Temperature Rise and Demagnetization Considered," *IEEE Access*, Vol. 9, May 2021, pp. 64761–64775. https://doi.org/10.1109/ACCESS.2021.3076228.

[44] Jurković, M., and Žarko, D., "Optimized Design of a Brushless DC Permanent Magnet Motor for Propulsion of an Ultra Light Aircraft," *Automatika*, Vol. 53, No. 3, 2012, pp. 244–254. https://doi.org/10.7305/automatika.53-3.114.

[45] Pulliam, T., Nemec, M., Holst, T., and Zingg, D., "Comparison of evolutionary (genetic) algorithm and adjoint methods for multi-objective viscous airfoil optimizations," *41st Aerospace Sciences Meeting and Exhibit*, 2003, p. 298.

[46] Rios, L. M., and Sahinidis, N. V., "Derivative-free optimization: a review of algorithms and comparison of software implementations," *Journal of Global Optimization*, Vol. 56, 2013, pp. 1247–1293.

[47] Martins, J. R. R. A., and Ning, A., *Engineering design optimization*, Cambridge University Press, 2021.

[48] Babcock, T., Bedonian, G., and Hicken, J. E., "Multidisciplinary analysis of propulsive electric motors during takeoff," *AIAA Scitech 2021 Forum*, 2021, p. 1778.

[49] Martins, J. R., Alonso, J. J., and Reuther, J. J., "High-fidelity aerostructural design optimization of a supersonic business jet," *Journal of Aircraft*, Vol. 41, No. 3, 2004, pp. 523–530.

[50] Martins, J. R., Alonso, J. J., and Reuther, J. J., "A coupled-adjoint sensitivity analysis method for high-fidelity aero-structural design," *Optimization and Engineering*, Vol. 6, 2005, pp. 33–62.

[51] Kenway, G. K., and Martins, J. R., "Multipoint high-fidelity aerostructural optimization of a transport aircraft configuration," *Journal of Aircraft*, Vol. 51, No. 1, 2014, pp. 144–160.

[52] Kennedy, G. J., and Martins, J. R., "A parallel aerostructural optimization framework for aircraft design studies," *Structural and Multidisciplinary Optimization*, Vol. 50, 2014, pp. 1079–1101.

[53] Gray, J. S., and Martins, J. R., "Coupled aeropropulsive design optimisation of a boundary-layer ingestion propulsor," *The Aeronautical Journal*, Vol. 123, No. 1259, 2019, pp. 121–137.

[54] Yildirim, A., Gray, J. S., Mader, C. A., and Martins, J. R., "Aeropropulsive design optimization of a boundary layer ingestion system," *AIAA Aviation 2019 Forum*, 2019, p. 3455.

[55] Abdul-Kaiyoom, M. A. S., Yildirim, A., and Martins, J. R., "Coupled Aeropropulsive Design Optimization of an Over-Wing Nacelle Configuration," *AIAA SCITECH 2023 Forum*, 2023, p. 0327.

[56] Burghardt, O., Gauger, N. R., Gomes, P., Palacios, R., Kattmann, T., and Economon, T. D., "Coupled discrete adjoints for multiphysics in su2," *AIAA AVIATION 2020 FORUM*, 2020, p. 3139.

[57] Anibal, J. L., Mader, C. A., and Martins, J. R., "Aerodynamic shape optimization of an electric aircraft motor surface heat exchanger with conjugate heat transfer constraint," *International Journal of Heat and Mass Transfer*, Vol. 189, 2022, p. 122689.

[58] Hanselman, D., *Brushless Permanent Magnet Motor Design*, Magna Physics Publishing, 2003.

[59] Haimes, R., and Dannenhoffer, J., *The Engineering Sketch Pad: A Solid-Modeling, Feature-Based, Web-Enabled System for Building Parametric Geometry*, 2013. https://doi.org/10.2514/6.2013-3073.

[60] Haimes, R., and Drela, M., *On The Construction of Aircraft Conceptual Geometry for High-Fidelity Analysis and Design*, 2012. https://doi.org/10.2514/6.2012-683.

[61] Haimes, R., Dannenhoffer, J., Bhagat, N. D., and Allison, D. L., *Multi-fidelity Geometry-centric Multi-disciplinary Analysis for Design*, 2016. https://doi.org/10.2514/6.2016-4007.

[62] Chen, J., Wang, D., Cheng, S., Jiang, Y., Teng, X., Chen, Z., Shen, Y., Birnkammer, F., and Gerling, D., "A hysteresis model based on linear curves for NdFeB permanent magnet considering temperature effects," *IEEE Transactions on Magnetics*, Vol. 54, No. 3, 2017, pp. 1–5.

[63] "Sintered neodymium-iron-boron magnets - arnold magnetic technologies," , 2017. URL https://www.arnoldmagnetics.com/wp-content/uploads/2017/11/N48H-151021.pdf.

[64] Kolev, T. V., "Modular Finite Element Methods," Computer Software, mfem.org, feb 2020. https://doi.org/10.11578/dc.20200303.5.

[65] Anderson, R., Andrej, J., Barker, A., Bramwell, J., Camier, J.-S., Dobrev, J. C. V., Dudouit, Y., Fisher, A., Kolev, T., Pazner, W., Stowell, M., Tomov, V., Akkerman, I., Dahm, J., Medina, D., and Zampini, S., "MFEM: A Modular Finite Element Methods Library," *Computers & Mathematics with Applications*, Vol. 81, 2021, pp. 42–74. https://doi.org/10.1016/j.camwa.2020.06.009.

[66] Falgout, R. D., and Yang, U. M., "hypre: A Library of High Performance Preconditioners," *Computational Science — ICCS 2002*, edited by P. M. A. Sloot, A. G. Hoekstra, C. J. K. Tan, and J. J. Dongarra, Springer Berlin Heidelberg, Berlin, Heidelberg, 2002, pp. 632–641.

[67] Henson, V. E., and Yang, U. M., "BoomerAMG: A parallel algebraic multigrid solver and preconditioner," *Applied Numerical Mathematics*, Vol. 41, No. 1, 2002, pp. 155–177. https://doi.org/10.1016/S0168-9274(01)00115-5.

[68] Fatemi, A., Ionel, D. M., Demerdash, N. A. O., Staton, D. A., Wrobel, R., and Chong, Y. C., "Computationally Efficient Strand Eddy Current Loss Calculation in Electric Machines," *IEEE Transactions on Industry Applications*, Vol. 55, No. 4, 2019, pp. 3479–3489. https://doi.org/10.1109/TIA.2019.2903406.

[69] Sullivan, C. R., "Computationally efficient winding loss calculation with multiple windings, arbitrary waveforms, and two-dimensional or three-dimensional field geometry," *IEEE transactions on power electronics*, Vol. 16, No. 1, 2001, pp. 142–150.

[70] Kennedy, G. J., and Hicken, J. E., "Improved constraint-aggregation methods," *Computer Methods in Applied Mechanics and Engineering*, Vol. 289, 2015, pp. 332–354. https://doi.org/10.1016/j.cma.2015.02.017.

[71] Coulomb, J., "A methodology for the determination of global electromechanical quantities from a finite element analysis and its application to the evaluation of magnetic forces, torques and stiffness," *IEEE Transactions on Magnetics*, Vol. 19, No. 6, 1983, pp. 2514–2519. https://doi.org/10.1109/TMAG.1983.1062812.

[72] Coulomb, J., and Meunier, G., "Finite element implementation of virtual work principle for magnetic or electric force and torque computation," *IEEE Transactions on Magnetics*, Vol. 20, No. 5, 1984, pp. 1894–1896. https://doi.org/10.1109/TMAG.1984.1063232.

[73] Gray, J. S., Hwang, J. T., Martins, J. R. R. A., Moore, K. T., and Naylor, B. A., "OpenMDAO: An open-source framework for multidisciplinary design, analysis, and optimization," *Structural and Multidisciplinary Optimization*, Vol. 59, No. 4, 2019, pp. 1075–1104. https://doi.org/10.1007/s00158-019-02211-z.

[74] Lambe, A. B., and Martins, J. R. R. A., "Extensions to the Design Structure Matrix for the Description of Multidisciplinary Design, Analysis, and Optimization Processes," *Structural and Multidisciplinary Optimization*, Vol. 46, 2012, pp. 273–284. https://doi.org/10.1007/s00158-012-0763-y.

[75] Hogan, R. J., "Fast reverse-mode automatic differentiation using expression templates in C++," *ACM Transactions on Mathematical Software (TOMS)*, Vol. 40, No. 4, 2014, pp. 1–16.

[76] Saad, Y., and Schultz, M. H., "GMRES: A generalized minimal residual algorithm for solving nonsymmetric linear systems," *SIAM Journal on scientific and statistical computing*, Vol. 7, No. 3, 1986, pp. 856–869.

[77] Martins, J. R. R. A., and Hwang, J. T., "Review and Unification of Methods for Computing Derivatives of Multidisciplinary Computational Models," *AIAA Journal*, Vol. 51, No. 11, 2013, pp. 2582–2599. https://doi.org/10.2514/1.J052184.

[78] Hwang, J. T., and Martins, J. R. R. A., "A Computational Architecture for Coupling Heterogeneous Numerical Models and Computing Coupled Derivatives," *ACM Trans. Math. Softw.*, Vol. 44, No. 4, 2018. https://doi.org/10.1145/3182393.

[79] Gill, P. E., Murray, W., and Saunders, M. A., "SNOPT: An SQP Algorithm for Large-Scale Constrained Optimization," *SIAM Journal on Optimization*, Vol. 12, No. 4, 2002, pp. 979–1006. https://doi.org/10.1137/S1052623499350013.

[80] Gill, P. E., Murray, W., and Saunders, M. A., "SNOPT: An SQP Algorithm for Large-Scale Constrained Optimization," *SIAM Review*, Vol. 47, No. 1, 2005, pp. 99–131. https://doi.org/10.1137/S0036144504446096.

[81] Wu, N., Kenway, G., Mader, C. A., Jasa, J., and Martins, J. R. R. A., "pyOptSparse: A Python framework for large-scale constrained nonlinear optimization of sparse systems," *Journal of Open Source Software*, Vol. 5, No. 54, 2020, p. 2564. https://doi.org/10.21105/joss.02564.

[82] Wieserman, W. R., Schwarze, G. E., and Niedra, J. M., "Comparison of High Temperature, High Frequency Core Loss and Dynamic B-H Loops of a 2V-49Fe-49Co and a Grain Oriented 3Si-Fe Alloy," SAE Tech. Pap. 929116, 1992. https://doi.org/10.4271/929116.